Supporting Information:

Van der Waals epitaxy growth of 2D ferromagnetic Cr$_{(1+\delta)}$Te$_2$ nanolayers with concentration-tunable magnetic anisotropy

Kinga Lasek,[1] Paula M. Coelho,[1] Pierluigi Gargiani,[2] Manuel Valvidares,[2] Katayoon Mohseni,[3] Holger L. Meyerheim,[3] Ilya Kostanovskiy,[3] Krzysztof Zberecki,[4] Matthias Batzill[1]

[1] Department of Physics, University of South Florida, Tampa, FL 33620, USA

[2] ALBA Synchrotron Light Source, E-08290 Cerdanyola del Vallès, Barcelona, Spain

[3] Max-Planck-Institut f. Mikrostrukturphysik, Weinberg 2, D-06120 Halle, Germany

[4] Faculty of Physics, Warsaw University of Technology, ul. Koszykowa 75, Warsaw, 00-662 Poland

I. Structural and compositional analysis by grazing incidence x-ray diffraction

First, line scans in reciprocal space were carried out to derive the metric of the Cr_xTe_y film relative to the MoS_2 substrate, the latter being characterized by lattice parameters a=b=3.163 Å, c=12.30 Å. Fig. S1(a) shows a line scan along the reciprocal a* axis (h) at k=0, and l=1.91 reciprocal lattice units (rlu) where the film peak has its maximum [see Fig. S1(b)]. The strong peak at h=1 is related to the (102) bulk reflection of the MoS_2 substrate. The weaker reflections at h≈0.80 and h≈1.60 rlu are related to the film structure and are indexed at (201) and (204) with respect to the (2×1) superlattice unit cell of the film. The peak at h≈1.40 rlu is attributed to a spurious reflection from a randomly oriented MoS_2 crystallite, which are frequently observed. The (301) reflection at h=1.20 rlu is too weak to be detected in this scan and is shown in the inset of Fig. S1(b). The 2x1 superstructure reflections are generally at least one order of magnitude weaker than those of the (1×1) structure as they are primarily due to the intercalated Cr atoms only. Fig. S1(b) shows a scan along the reciprocal c* axis at (hk)=(20) of the film which passes the first, second and third reflection order along q_z. Based on the reflection positions with respect to those of the MoS_2 substrate the lattice metric of the (2x1) unit cell is derived to be equal to a=7.90 Å, b=3.95 Å, c=6.43 Å. From the full width at half maximum (FWHM) of the reflections along c* (FWHM≈0.32 rlu) we estimate a film thickness of about t≈37 Å, i.e. the film is six triple layers thick, close to the nominal film thickness derived from the growth rate.
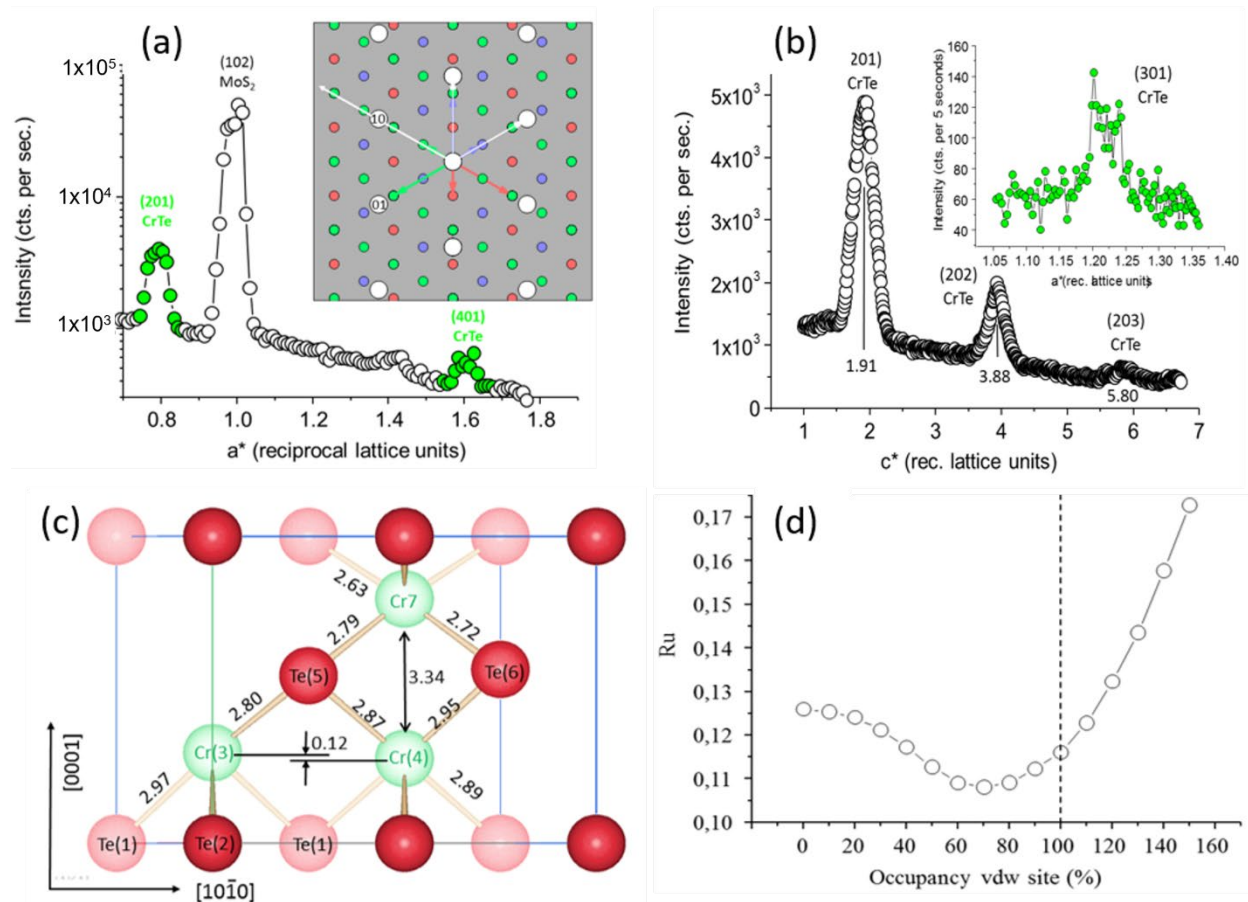
FIG. S1: XRD analysis of 6-7 layer $Cr_{(1+\delta)}Te_2$ film. (a) Scan along the a*-axis of the MoS_2 (0001) substrate at k=0 and l=1.91. The most intense maximum at h=1 is related to the (102) reflection of MoS_2. Reflections related to the Cr_xTe_y film are found at h=0.80 and h=1.60, which are indexed as (201) and

(401) based on the (2x1) superlattice unit cell of the film, respectively. The inset shows the reciprocal space within the a*-b* plane. White spheres indicate the reciprocal lattice point of the MoS$_2$ substrate while the small colored ones (green, red and blue) represent lattice points of the three different domains. The white arrow indicates the scan direction. (b): Scan along c* at the (hk)=(20) film reflection. Peaks are found at c*≈1.91, 3.88 and 5.80 reciprocal lattice units, which correspond to the first, second and third order reflections of the film along q$_z$. The reflection indices are indicated next to the reflections. The inset shows the (301) reflection of the film. These reflections with h being an odd number are at least one order of magnitude weaker than those related to the average (1x1) structure. (c) Schematic view of one (2x1)-Cr$_x$Te$_y$ unit cell as derived from the XRD structure refinement. The unit cell is shown with the (10$\overline{1}$0) face to the viewer. Red and green balls represent Te and Cr atoms, respectively. Numbers indicate distances in Ångstrøm units. Atoms are labeled according to Table (a). (d) Unweighted residuum versus occupancy (Θ) of the Cr vdW site within the (2x1) unit cell. The minimum is achieved near Θ=70%. We estimate the uncertainty to lie in the 10-20 percentage points regime. The dashed line indicates the maximum occupancy of 100% which is physically reasonable.

Integrated reflection intensities were collected by using a six-circle x-ray diffractometer operated in the z-axis mode[1] by rotating the sample around the surface normal (φ-scan) while the position of the 2-dimensional (2D) pixel detector was kept fixed at the in-plane (δ) and out-of-plane (γ) angle associated to each reflection (HKL) **Error! Bookmark not defined.**. In total 37 reflections were collected which reduce to 21 symmetry independent ones by averaging over equivalent reflections based on the 3m point group symmetry of the unit cell (out of plane momentum transfer q$_z$ limited to q$_z$>0). The average agreement between symmetry equivalent reflections was 15%, which - given the large fraction of weak reflections - is a reasonable agreement.

The high resolution XRD, is used to refine the crystal structure and to determine occupation of the intercalation site. According to the P3m1 space group (SGR) symmetry (SRG Nr. 156)[2] of the unit cell, the atoms Te, Cr and Te occupy high-symmetric Wyckoff positions, namely (1a) at (00z), (1b) at ($^1/_3$ $^2/_3$ z) and (1c) at ($^2/_3$ $^1/_3$ z). In addition, we have considered the partially occupied intercalation sire at ($^1/_3$ $^2/_3$ z) directly above the Cr atoms in the TMD layers. Since this site is assumed to be occupied only in every other unit cell, fractional half order reflections appear which in the (2x1) metric of the unit cell correspond to those in which the reflection index h is an odd number. The (2x1) unit cell is then modeled by doubling the unit cell along the a-axis while keeping the lateral position of the atoms (x, y) at their fixed high symmetry positions within the a-b-plane, while the z-positions are allowed to vary. In addition, the incoherent superposition of the diffraction patterns originating from three domains was taken into account. Structural refinement was carried out by least squares refinement of the calculated squared structure factor magnitudes, ($|F(HKL)_{calc}|^2$) to the observed ones ($|F(HKL)_{obs}|^2$) using the Program Prometheus[3]. The observed squared structure factor magnitudes, $|F(HKL)_{obs}|^2$, were derived from the integrated intensities by multiplying with instrumental factors (Lorentz, polarization- and effective area)[4,5]. Fig. S2(c) shows the structure model derived from the best fit whose quality is measured by the un-weighted residuum given by: Ru=$\sum(|I_{obs}|-I_{cal}|)/\sum I_{obs}$, where I$_{obs}$ and I$_{cal}$ correspond to the observed and calculated intensity, respectively. We derive Ru=0.108, which is a very good value.

The refined crystal structure is shown in Fig S1(c). Interatomic distances in the refined structure are within the range of 2.63 Å (minimum) and 2.97 Å (maximum), which is at most only varying 5% from the Cr-Te distance found in bulk Cr$_x$Te$_y$ compounds (2.71 Å). In addition, the occupation of the intercalated Cr sites, labeled as Cr(7), has been varied to improve the Ru. Fig. S1(d) shows a plot of Ru versus the fractional occupancy (Θ) of this site. We find a clear minimum near Θ≈70±15%, while Ru increases for both lower

and higher values of Θ. Here $\Theta=100\%$ corresponds to all Cr-interstitial sites in a 2x1 structure occupied, i.e. $\delta=0.5$. Therefore, the XRD analysis gives an intercalation occupation of $\delta=0.38\pm0.05$, which is less than the value measured in RBS (discussed below). The intercalated Cr atom (Cr7) is located directly above a Cr atom [Cr(4)] in the TMD layer at a distance of 3.34 Å. This relatively large distance and the vertical relaxation of the other atoms in the unit cell are attributed to the repulsion between the Cr atoms.

We also note that the structure refinement includes the full consideration of the atomic displacement parameters (ADP's) listed in Tabel S1[6]. For the different groups of atoms [(1,2), (3,4), (5,6) and (7)] we have used the same anisotropic values (U^{ii}), which are found to be very large, the range of 0.2-0.3 Å^2. These large values can only be static in nature which is directly imaged by scanning tunneling microscopy (STM).

Atom	x	y	z	U^{11}(Å^2)	U^{33}(Å^2)	Θ	
Te(1)	0	0	0	0.30	0.30	1.00	
Te(2)	1/2	0	0	0.30	0.30	1.00	
Cr(3)	1/6	2/3	0.29	0.24	0.24	1.00	
Cr(4)	2/3	2/3	0.27	0.24	0.24	1.00	
Te(5)	1/3	1/3	0.54	0.03	0.29	1.00	
Te(6)	5/6	1/3	0.56	0.03	0.29	1.00	
Cr(7)	2/3	2/3	0.79	0. 06	0.06	0.70	

TABLE S1 Coordinates (x, y, z), mean squared displacement amplitudes (U^{ii}), occupancy factors (Θ) of all atoms within the (2x1) unit cell with lattice parameters a=7.90 Å, b=3.95 Å, c=6.43 Å. Labels of the atoms refer to Fig. S1(c). Standard deviations are about ±0.02 for the coordinates and ±0.05 for U^{ii}

II. Compositional analysis by Rutherford Backscattering Spectroscopy (RBS)

Rutherford Backscattering Spectroscopy was performed on the $Cr_{(1+\delta)}Te_2$ thin film samples using He^+ beam produced by the commercial NEC Pelletron ion accelerator. An ion beam of 1.9MV and 40nA current was hitting the sample tilted by 9° in order to avoid channeling geometry. Backscattered spectra were collected by the Amptek implanted detector with the energy resolution of 16kV at 169° scattering angle. Total dose of 40 μCdefined by the charge integration circuit was collected. Fig. S2 shows the RBS spectrum with marked elemental edges for Mo, S, Cr and Te atoms. Thin film of Cr and Te atoms are forming two peaks on the spectrum, while the substrate atoms are represented by the semi-infinite edges for Mo and S. We performed the analysis of the RBS data with SimNRA code and found total atomic densities for total Cr and Te content: Cr – 2.0×10^{16} atoms/cm², Te – 7.0×10^{16} atoms/cm². Unfortunately, the resolution of the RBS detector does not allow to differentiate Te content in a Te- capping and in the layer. Thus, two additional approaches were used to obtain reliable Cr:Te ratios of the film: (a) High Resolution RBS (HRBS) and (b) using a platinum capping layer on some films instead of the tellurium capping. These measurements are illustrated next.
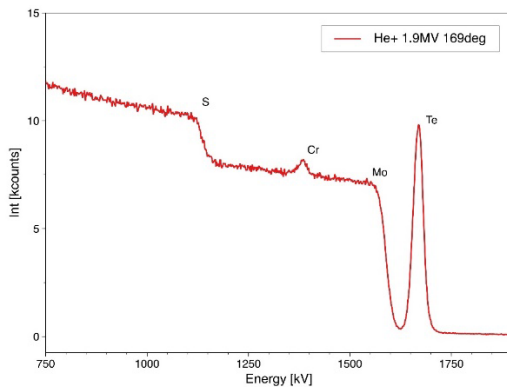
FIG. S2: Rutherford back scattering of a tellurium capped sample. The Te from the capping layer cannot be separated from the Te in the film and thus regular RBS does not allow to determine the film composition for samples with Te capping.

II.A High-resolution RBS

HRBS is measured by the commercial HRBS detection system (NEC), that consists of the magnetic spectrometer and 10cm MCP detector. HRBS data was collected with a 400kV He+ beam, at which the backscattering cross-section is close to its maximum. HRBS geometry is fixed at 90° scattering angle, where a low beam energy improves surface sensitivity as compared with regular RBS measurements. The incident and reflected angles of the beam relative to the sample normal were 45°. The configuration of the HRBS system provides an access to the small energy region with the higher energy resolution. The mean energy of the selected range is defined from the magnet current. The energy range is about +/-10% of the mean energy. To perform the conversion from the MCP position data into the energy scale, the calibration of the magnetic spectrometer and the MCP detector was using elemental thin films of Au and Ag on Si.

Fig S3 shows HRBS data collected with the detector magnet set for 29A, which is equivalent to 330kV mean detector energy. The tellurium peak is clear in the field of view. The contributions from the layers

and the Te-capping can be directly estimated. The spectrum provides an accurate intensity ratio: capping 60% and layer 40%. If we assume total atomic density of Te from the RBS experiment (7×10^{16} atoms/cm^2), we get Te content in the layer of 2.8×10^{16} atoms/cm^2. The atomic layer stoichiometry is thus $Cr_2Te_{2.8}$ or effectively $Cr_{1.44}Te_2$, for this sample.
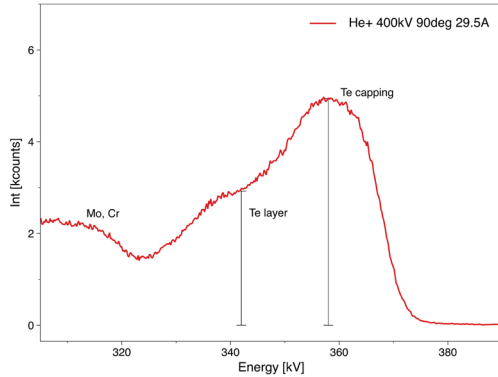
FIG. S3: High resolution RBS allows separation of Te in the film from a Te capping layer.

Fig. S4 shows HRBS spectrum measured at 28A magnet current – 297kV mean energy. At this energy the Mo edge and Cr peak are in the field of view. From the Te peak, only the layer component is present. The grey area represents the boundary region on the edge of the MCP, where the signal rapidly decays. Experimental data was fitted using SimNRA code. Color dots represent single components in the total fitting curve shown with the blue line. Black arrows mark the position of the Mo edge intensity oscillations in the close to channeling geometry. The fitting results in the $Cr_{1.46}Te_2$ stoichiometry are in a good agreement with previously discussed data.
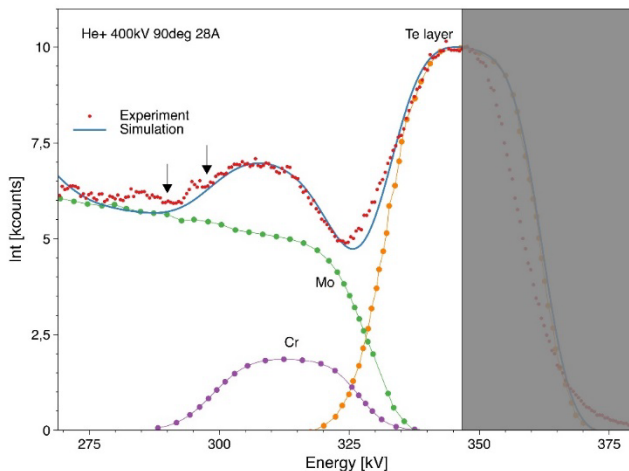
FIG. S4: HRBS spectrum measured with 297kV mean energy to allow monitoring Cr, Mo and Te edge to determine the film composition. For tellurium only the component from the Cr-telluride film is present but not the capping layer.

II.B RBS and HRBS with Pt capping layer

To avoid the error in composition estimation caused by overlapping contributions of Te from the film and the capping layer an extra set of samples capped with Pt film was prepared. The scattering from the heavy Pt is clearly separated from all the other sample peaks and this allows compositional analysis of the film in both regular RBS and HRBS. Fig. S5

shows HRRBS of two such samples with different post-growth annealing temperatures.
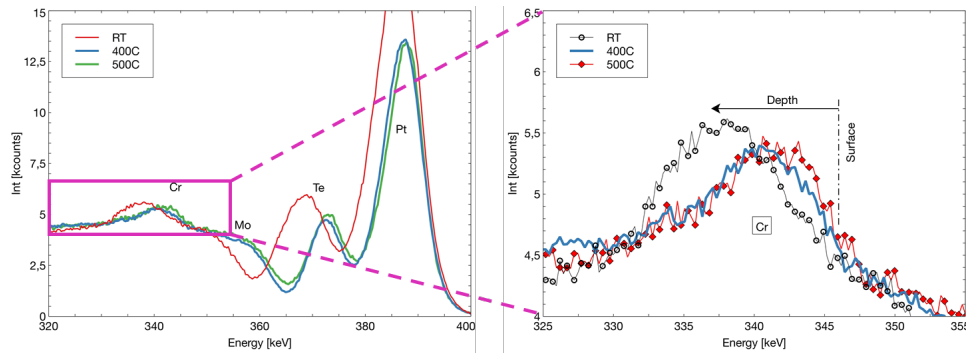
FIG. S5: HRBS spectrum measured on as grown and post growth annealed films capped with Pt film. The separation of the Pt-capping layer from the scattering peaks of the film now allows for a compositional analysis of the film.

II.C RBS summary

In total four samples were characterized by RBS/HRRBS. Wherever possible RBS and HRRBS gave very similar compositions. Two as grown samples and two samples after post-growth annealing were studied. Table S2 summarizes the results. It is apparent that films grown between 200 and 350 ˚C have similar composition of around 1.54± 0.10 while samples annealed after growth to above 400 ˚C have a higher composition close to that of Cr-monotelluride.

Table S2. Film composition evaluated from RBS measurements.

$Cr_{1+\delta}Te_2$	Growth at 200 °C	Growth at 350 °C	Annealed at 400 °C	Annealed at 500 °C
Concentration	$Cr_{1.64}Te_2 \pm 0.02$	$Cr_{1.44}Te_2 \pm 0.025$	$Cr_2Te_2 \pm 0.02$	$Cr_{2.1}Te_2 \pm 0.02$

III. STM characterization of growth spirals for films grown at 350 ˚C.

The growth spirals that form for films grown at elevated temperatures (350 ˚C) are not a full-layer height, but half-layer terrace steps with 0.3 nm height are observed, as shown in the line-scan in Fig. S6 (a). Moreover, terraces with such a half layer height also exhibit a (defective) 1x1 structure in STM, as shown in Fig. S6(c). The step height and the atomic structure suggest that these growth spirals are formed by a partial dislocation and the terraces are forming a Cr-monotelluride layer on top of the $CrTe_2$-TMD layer as schematically illustrated in the inset of Fig. S6(b). As we follow the terrace around the screw dislocation, the 1x1 atomic structure changes to the regular 2x1 structure and the step height increases to a regular monolayer height, i.e., 0.6 nm. This may indicate that the spiral growth proceeds via half a TMD layer that then converts into a full TMD layer with intercalated Cr as the spiral grows.
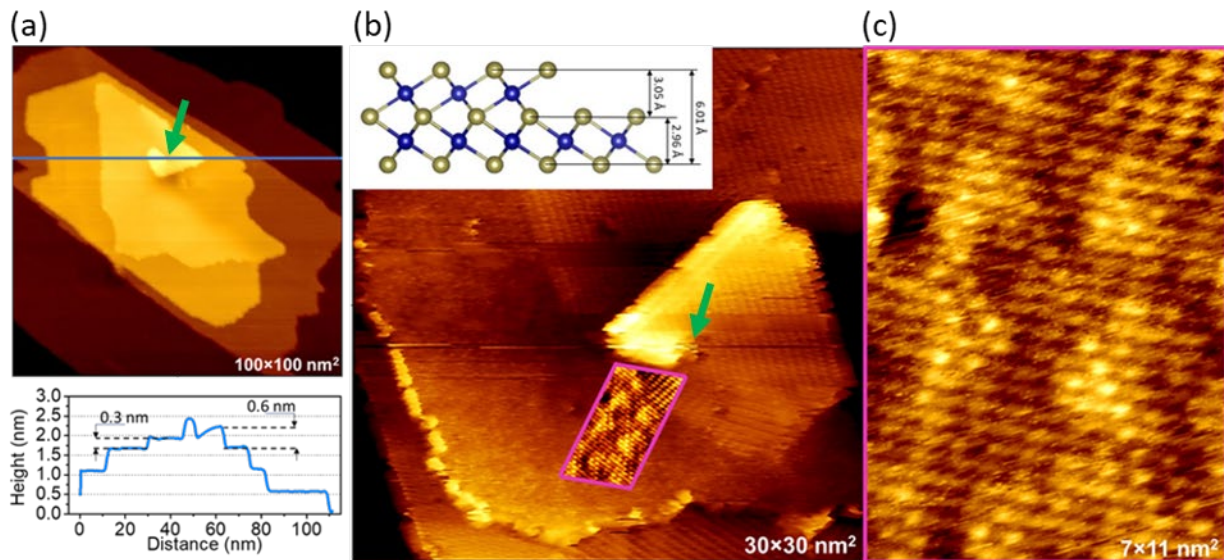
FIG. S6. Screw dislocations (marked by green arrows) in few-layer thick Cr-telluride film grown at elevated temperatures. Spiral like growth of the film is shown on large scale STM image (a). Line profile reveals two different step heights i.e., 0.3 nm and 0.6 nm, the latter corresponding to a full TMD layer. These half layer-height terraces exhibit 1×1 topography corrugation (b, c), suggesting the appearance of a Cr-Te bilayer. STM imaging conditions (sample bias, tunneling current): (a) large scale 1.2 V, 0.7 nA, (b) -0.2 V, 0.8 nA, (c) 0.1 V, 0.8 nA.

IV. Ultraviolet photoemission spectroscopy (UPS) of as grown and post growth annealed few layers thick $Cr_{(1+\delta)}Te_2$
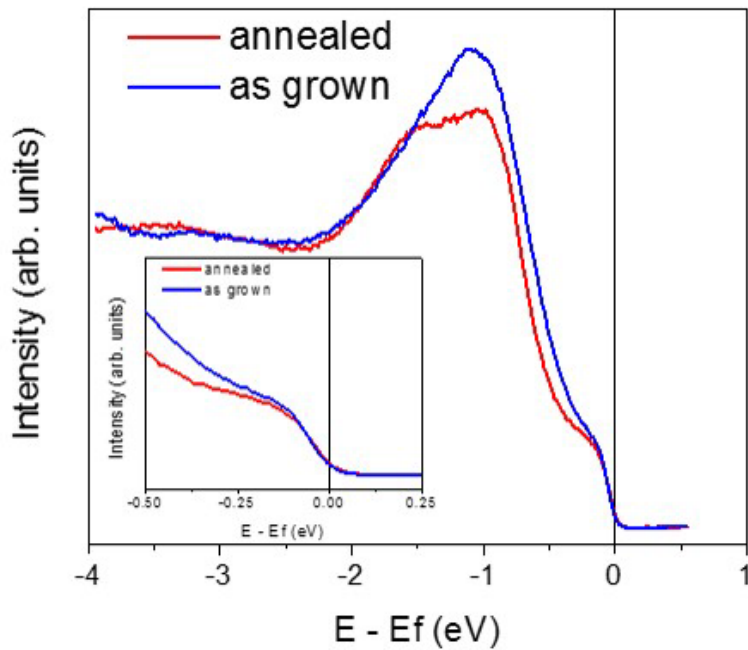
FIG. S7: Valence band photoemission spectra of Cr-Te film taken with a photon energy of 21.6 eV for a film grown at 300 ˚C and after vacuum annealing of the same film to 500 ˚C. The Fermi-level is set to 0 eV binding energy.

V. Magnetic moment evaluation from XMCD measurements

To obtain the spin and orbital magnetic moments from XMCD experiment the sum rule method has been applied.[7],[8] The p and q (Fig. S8(b)) and r shown in Fig. S8(a) are the three integrals needed in the sum rule analysis.[9] The magnetic orbital (m_l) and spin (m_s) moments can be calculated as $-4q(10 - n_{3d})/3r$ and $-(6p - 4q)(10 - n_{3d})/r$, respectively. Where n_{3d} is the 3d electron occupation number.

In order to apply the sum rule, distinguishable L_2 and L_3 edges and clear separation into $j_{3/2}$ and $j_{1/2}$ excitations are necessary.[10] In case of light transition metal $e.g.$ Cr the spin orbit splitting is strongly reduced and the jj mixing between the $2p_{3/2}$ and $2p_{1/2}$ appears. To overcome this problem the spin correction factor must be taken into account to consider the jj mixing between the $2p_{3/2}$ and $2p_{1/2}$. Lack of this correction can lead to the big m_l and spin m_s estimation errors. The spin correction factor reported for Cr varies between 1.4 and 2.3.[10]
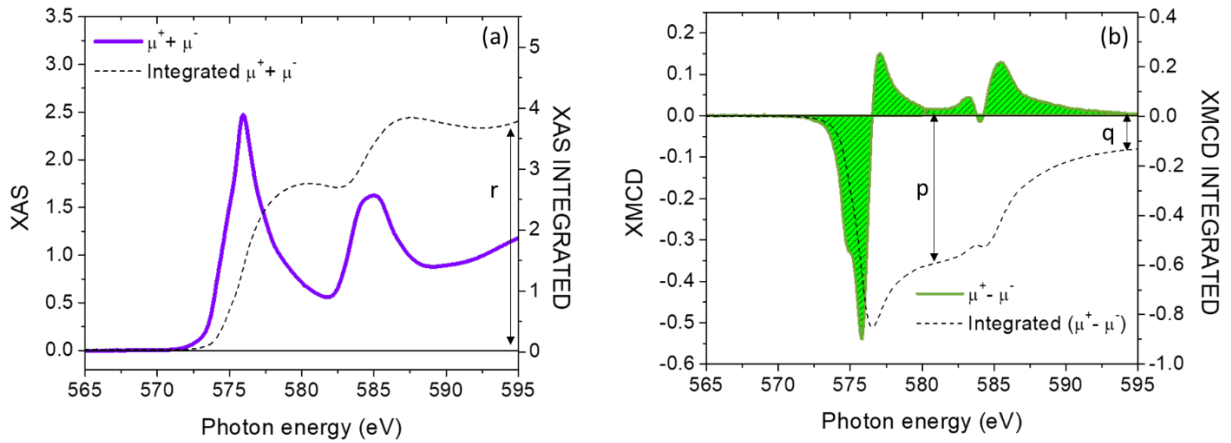
FIG. S8: $L_{2,3}$ – edge XAS and XMCD spectra of chromium: (a), (b) the XAS and XMCD absorption spectra and their integrations, respectively.

VI. Calculated projected density of states (PDOS) on atomic d states of Cr atoms in a four layer thick Cr$_{(1+\delta)}$Te$_2$ with (δ=1/2).
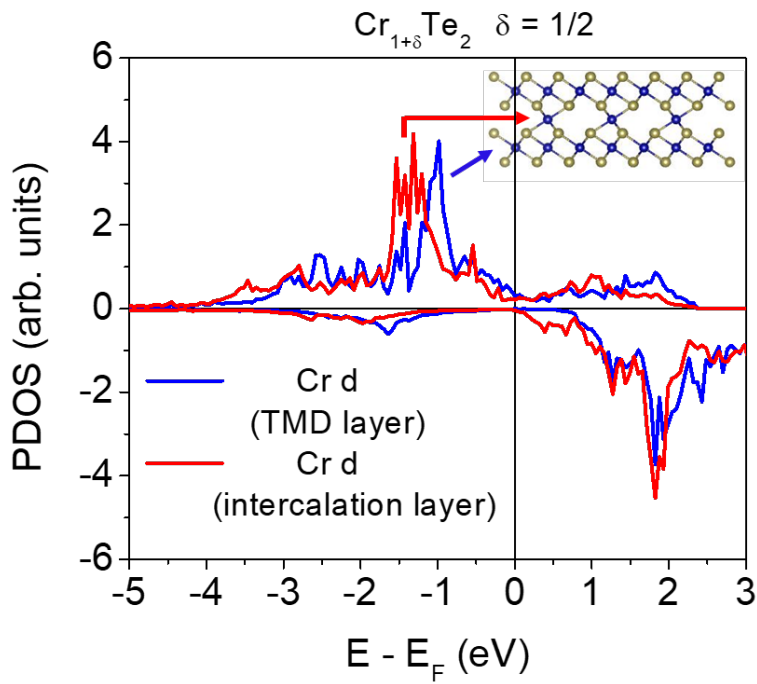
FIG. S9: PDOS on atomic d states of Cr atoms in the TMD layer (blue line) and intercalation layer (red line). The Fermi-level is set to 0 eV binding energy.

VII. Magnetic modifications of MoS$_2$ (comparison XMCD *vs.* VSM)

The magnetic properties measured by XMCD reflect only the magnetic response of Cr in the Cr$_{(1+\delta)}$Te$_2$ film and this has been the main goal of this study. However, in order to determine the properties of the 'entire volume' of the sample and allow comparison to more common magnetometry studies we also measured the magnetic properties of the samples using bulk sensitive VSM on the multilayer thick films. Unexpectedly, we observe a more complex M-H hysteresis in VSM compared to XMCD on the same samples. Fig. S10(a) present the superimposed normalized magnetization loops measured by VSM and XMCD for films grown at 350 °C. In VSM, the magnetic hysteresis loop exhibits an extra modulation compared to the Cr magnetization loop measured by element specific and surface sensitive XMCD. Measurements conducted with external magnetic field applied out of the sample plane using XMCD show a perfect match of coercive fields; however, VSM measurements reveal, a two-step magnetization character, suggesting that the sample may consist of two magnetic materials. This extra modulation vanishes in a temperature range of 150 - 200 K (Fig. S10(c)) which is very close to the Curie temperature of the Cr-telluride film obtained from XMCD experiments. Such high temperature excludes the possibility of the temperature lag being an origin of the observed differences in obtained data with these two techniques. Differences are also observed in the magnetization versus temperature measurements acquired by VSM and XMCD. In XMCD the Curie temperature (T$_c$) of the Cr-telluride film is determined to be close to 190 K, in VSM only a small kink in the M(T) curve is observed at this temperature (see arrow #1 in Fig. S10 (b)). A clear ferromagnetic-to-paramagnetic transition occurs at ~ 270 K (see arrow #2 in Fig. S10(b)) in VSM measurements; however, some weak saturation magnetization appears to remain up to above RT. Closer inspection of the Cr-XMCD signal shows that a small Cr magnetization is also still present in the temperature range between 190 and 270 K (highlighted by the circle in Fig. S10(b)). This indicates that the fairly strong magnetization measured by VSM, in this temperature range, may also have a contribution from Cr. The aforementioned kink observed in the VSM-M(T) data was also observed with an external field applied in the sample plane. Results presented in Fig. S10 (d) indicate an even stronger modulation of the M(T) curve in the same temperature range (~ 190 °C).

The overlap of two different M-H hysteresis loops in VSM clearly shows that there are two separate magnetic materials. Prior to deposition of the Cr telluride film the MoS$_2$ substrate did not exhibit any magnetic properties as the M-H curve of the clean substrate shown in Fig. S10(c) demonstrates. Thus, the growth of Cr telluride films appears to have magnetically modified the substrate. Diluted magnetic group VIB TMDs, including MoS$_2$, have been recently reported (see main text for references). Thus, we propose that Cr-diffusion into the substrate may cause the magnetic signal in VSM. The much-suppressed magnetic signal in Cr-XMCD in the temperature range between 190 and 270 K can have two possible explanations. Either the magnetic substrate induces a weak magnetism in the Cr-telluride film by proximity, or the weak signal is from diluted magnetic dopants in the MoS$_2$ substrate that induce the magnetism.
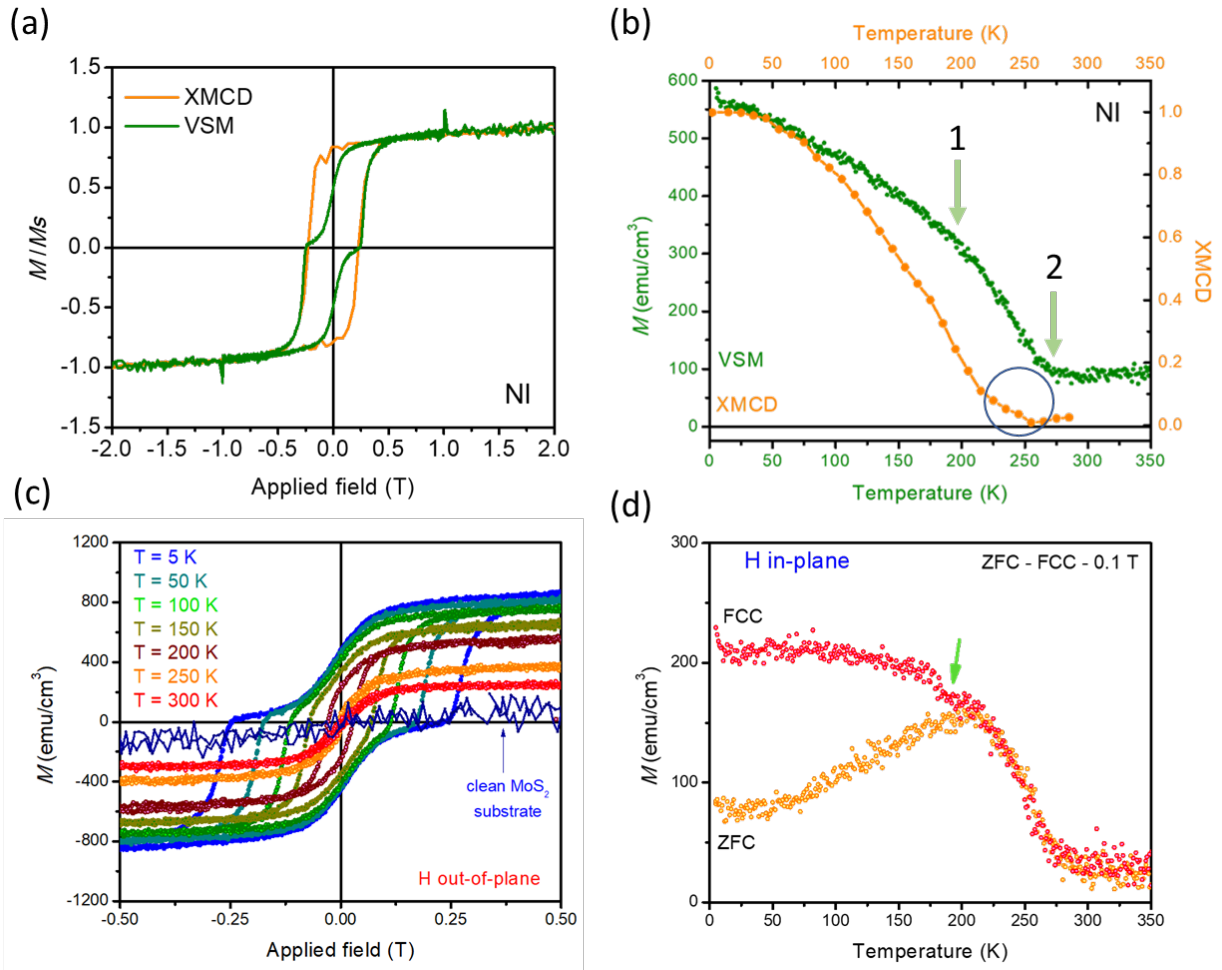
FIG. S10: Magnetic characterization of a few-layer thick Cr-telluride film by XMCD and VSM. (a) Normalized magnetization as a function of applied field measured at 2K for the field applied in NI direction. (b) temperature dependence of magnetization carried out in 50 mT (XMCD) and 100 mT (VSM) after field cooled preparation in 6T. (c) Magnetization as a function of applied field performed at various temperatures as indicated in the figure. (d) temperature dependence of magnetization measured by VSM with 0.1 T of applied external field in the sample plane.

Detailed studies of the magnetization curves measured by VSM under different values of applied magnetic field (0.02, 0.05, and 0.1 T) are presented in Fig. S11. The obtained field cooled curves reflect a typical magnetization behavior of a ferromagnetic film. The ZFC curves, however, show an increase of magnetic moment upon increasing temperature from 5K, followed by a decrease of the magnetic moment after a peak at a characteristic temperature, and eventually merge with the FCC curve at a blocking temperature T_B. Moreover, with an increasing magnetic field, the decrease of the blocking temperature is observed. This behavior is characteristic for materials with spin-glass properties. We cannot say unequivocally though if the $Cr_{(1+\delta)}Te_2$ films have a clear signature of a spin-glass material. The observed bifurcation of the ZFC and FC curves may instead be an indication of the coexistence of ferromagnetic and

antiferromagnetic coupling in the films. This phenomenon requires further studies that go beyond the scope of this manuscript.
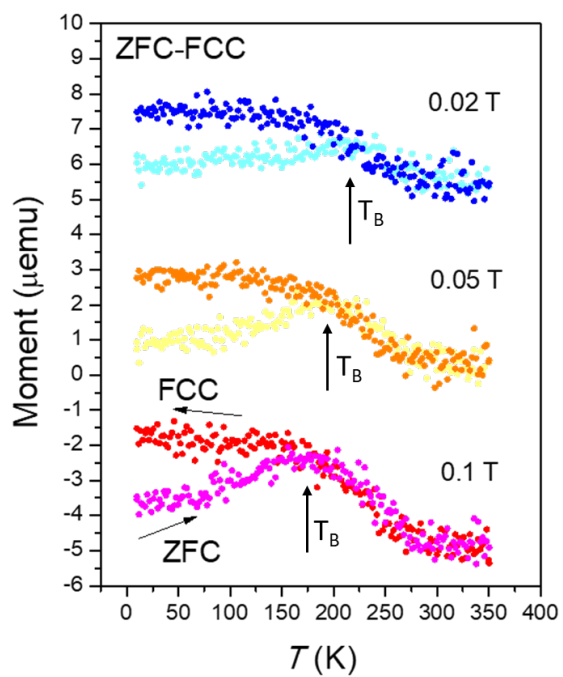
FIG. S11: VSM zero field cooled and field cooled curves of a few layers thick Cr-telluride film grown at 350 °C.

Supplement References:

[1] Vlieg, E. and Lohmeier M., Angle Calculations for a Six-Circle Surface X-ray Diffractometer. *J. Appl. Cryst.* **26**, 706 (1993).

[2] International Tables for Crystallography. Volume A, Space-Group Symmetry. Dordrecht; London: Published for the International Union of Crystallography by Kluwer Academic Publishers, (2002).

[3] Zucker, U. H., Perenthaler, E. W., Kuhs, F., Bachmann, R. and Schulz, H., A program system for investigation of anharmonic thermal vibrations in crystals. *J. Appl. Cryst*. **16**, 358 (1983).

[4] Schamper, C. Meyerheim, H. L.; and Moritz, W. Resolution correction for surface X-ray diffraction at high beam exit angles. *J. Appl. Cryst*. **26**, 687 (1993).

[5] Vlieg, E., Integrated Intensities Using a Six-Circle Surface X-ray Diffractometer. *J. Appl. Cryst*. **30**, 532 (1997).

[6] Kuhs, W. F., Generalized Atomic Displacements in Crystallographic Structure Analysis. *Acta Cryst*. **A48**, 80, (1992).

[7] Thole, B.; Carra, P.; Sette, F.; van der Laan, G. X-ray circular dichroism as a probe of orbital magnetization. *Phys. Rev. Lett*. **68**, 1943 (1992).

[8] Carra, P., Thole, B.; Altarelli, M.; Wang, X. X-ray circular dichroism and local magnetic fields. *Phys. Rev. Lett*. **70**, 694 (1993).

[9] Chen, C.; Idzerda, Y.; Lin, H.-J.; Smith, N.; Meigs, G.; Chaban, E.; Ho, G.; Pellegrin, E.; Sette, F. , Experimental confirmation of the X-ray magnetic circular dichroism sum rules for iron and cobalt. *Phys. Rev. Lett*. **75**, 152 (1995).

[10] Goering, E. J. P. M., X-ray magnetic circular dichroism sum rule correction for the light transition metals. Philosophical Magazine, **85**, 2895 (2005).